

# Transmission electron microscopy

**Lluís López-Conesa\***

Universitat de Barcelona

lluis.lopez.conesa@ub.edu

**Abstract:** This work aims at giving a general overview of transmission electron microscopy, from the beginnings of the technique in the 1930s to the latest technological advances and their relevance to current research. The focus is an attempt at explaining the different physical mechanisms that allow obtaining structural and compositional information from the observed object by studying its interaction with a beam of accelerated electrons.

**Keywords:** transmission electron microscopy, resolution, contrast, spectroscopy, nanoscience, nanotechnology.

**Resum:** Aquest treball vol oferir una visió general de la microscòpia electrònica de transmissió, partint d'un repàs històric des dels inicis de la tècnica els anys 30 del segle xx fins arribar als darrers avenços i la seva rellevància en el context de la recerca actual. Es posa l'èmfasi en intentar explicar els diferents mecanismes físics que permeten obtenir informació estructural i composicional de l'objecte observat a partir de la seva interacció amb un feix d'electrons accelerats.

**Paraules clau:** microscòpia electrònica de transmissió, resolució, contrast, espectroscòpia, nanociència, nanotecnologia.

\* Lluís López Conesa is an associate professor with the UB Department of Electronic and Biomedical Engineering and a technician with the unit for TEM applied to materials of the Scientific and Technological Centers of the University of Barcelona (CCiTUB). His main lines of research are focused on the development of characterization techniques in transmission electron microscopy and their application, especially, to nanoscience and nanotechnology. ORCID: 0000-0003-1456-079X.

**Transmission electron** microscopes are tools that deal with shadows in a two-fold way. On a practical level, they rely on the image imprinted on a support by a beam after going through an object that partially blocks its path. On a more philosophical level, as with all microscopes, they allow us to peek into a shadow realm: that of what is too small to be seen by our naked eye.

## Historical overview of TEM

### What is resolution?

Microscopes have been used since the late 16th century in order to extend the resolution limit of the human eye. For most of this time, the illumination source used to obtain images was only visible light. But, in the early 20th century, the development of quantum mechanics and, in particular, the wave-particle duality proposed by De Broglie (1925), ultimately resulted in the development of an electron microscope by Ruska and Knoll (1931 and 1932).

Since the Rayleigh criterion for the resolution of two specific objects involves the wavelength of the illumination source, using highly accelerated electrons opened a resolution range which is unattainable to visible light microscopy. Whereas for the shortest range of the visible light spectrum the wavelength is = 400 nm, for electrons accelerated at 100keV it is = 4 pm. Using the magnetic field created by the current running through a copper coil as an electromagnetic lens to focus the electron beam coming from a thermionic source, Ruska and Knoll built the first transmission electron microscope (TEM) in 1931. The resolution achieved (in the hundreds of nm) was not diffraction-limited by the electron wavelength, but by the quality of the electron optics. Only two years after that, TEM had surpassed the resolution achievable with the visible light microscope.

Over time, the combination of technical improvements in electron optics and the use of higher accelerating voltages resulted in ever-increasing resolutions in TEM. Contrast fringes that could be related directly to the projected crystal potential were reported by Allpress, Sanders and Wadsley (1969). TEM has been since a key technique in the study of the structure of materials, being the only real space imaging technique for crystal structures and defects. Following the same basic layout of the Ruska and Knoll design, a major breakthrough was achieved in 1970 by Crewe with the development of the scanning mode of the TEM (STEM). In STEM, a narrow probe is formed by demagnifying the electron source on top of the speci-

men. This probe is then scanned across the specimen using the deflection coils. The detector picks up the signal coming from the interaction of the electron beam with a highly localized region of the sample. Following the reciprocity theorem stated by Cowley (1969), the STEM can be understood as a TEM with an interchanged source and detector. This mode is particularly suited to carrying out spectroscopic analyses, obtaining chemical information at the very high spatial resolution that the instrument offers.

### What can spectroscopy add to imaging?

Together with the STEM mode, the development of the field emission gun (FEG), also in the early 1970s, was a major breakthrough in spectroscopic techniques related to TEM. Their combination allowed the development of a narrow, very bright probe that could be accurately placed on the sample to obtain chemical signals with a sufficient signal to noise ratio in reasonable acquisition times. Two main spectroscopies are carried out in the TEM that allow for a quantitative analysis of chemical composition: energy-dispersive X-ray spectroscopy (EDS), and electron energy loss spectroscopy (EELS).

EDS analyzes the energies of the characteristic X-rays generated when the atoms in the sample return to their ground state after being ionized by the electron beam. Since each element presents its unique range of characteristic ionization energies, elemental identification is straightforward. Given that specimens suitable for TEM are particularly thin, X-ray absorption and fluorescence effects can be neglected and the relative atomic composition can be determined from ionization peak ratios, following the so-called Cliff-Lorimer technique.

EELS analyzes the energy loss distribution of electrons that have traveled through the sample. Different types of interactions of the impinging electron beam and the atoms of the sample give rise to different regions of the EEL spectrum. Most of the electrons come out of the sample without any detectable energy loss, and contribute to the so-called zero loss peak (ZLP), which is, by a few orders of magnitude, the most intense feature in the EEL spectrum. Next in energy loss appears the low-loss region (5 eV to 100 eV). This corresponds to the interaction of electrons in the beam with valence band electrons in the material. The main feature in this region is the plasmon peak. Since the plasmon energy (plasma frequency) is characteristic for each compound, chemical identification can be obtained. In addition, infor-

mation on optoelectronic properties of the material (band gap, complex dielectric function, interband and intraband transitions, etc.) can be extracted from the analysis of the energy loss distribution in this region. Also, the intensity ratio between the ZLP and the low-loss region can be used to determine the sample thickness. From 100 eV on, we find the core-loss region, corresponding to the interaction of electrons in the beam with core level electrons from atoms in the sample. Ionization edges are found at characteristic energy losses for each element; thus, elemental identification is straightforward. Quantitative composition determination is a more challenging task, but can also be achieved. The detailed methodology is described in Egerton's reference book in the field (2011). From the analysis of the core-loss fine structure (energy loss near edge structure, ELNES), quantitative information can also be obtained about the oxidation or bonding state of the atoms.

### Correcting aberrations

Scherzer proved theoretically back in 1936 that rotationally symmetric electromagnetic lenses could not be designed free of aberrations. Thus, a limit for the increase in resolution was expected for TEM. As a method to overcome this limitation, Scherzer himself proposed configurations for spherical aberration correctors in 1947. The technical chal-

lenge of their practical implementation becomes clear considering that the first demonstrated resolution improvement through the use of an aberration corrector in a TEM was achieved 50 years later, in 1997, by Haider and Rose. Figure 1 shows the evolution over time of visible light and electron microscopy, with a closer look at the recent improvements of TEM resolution. The range of length scales that has been opened to real space imaging in a very short period of time is remarkable.

Aberration correction is performed in electron optics in a different way than in visible light optics, since it is not possible to implement divergent electromagnetic lenses. The procedure consists, then, in measuring the aberrations present in a given configuration of the optical system and introducing opposite sign aberrations by using non-rotationally symmetric electromagnetic elements.

The use of aberration correction opened a new range of resolution both in TEM and STEM imaging and in spectroscopy, as well as allowing the use of lower voltages without loss of resolution. This results in a greater number of beam-sensitive materials becoming suitable for observation. State-of-the-art instrumentation is still improving, mainly through aberration corrector technology. Pushing resolution to the present limits imposes more demanding conditions on environmental variables, such as room temperature stability or mechanical isolation of the microscope, which need to improve

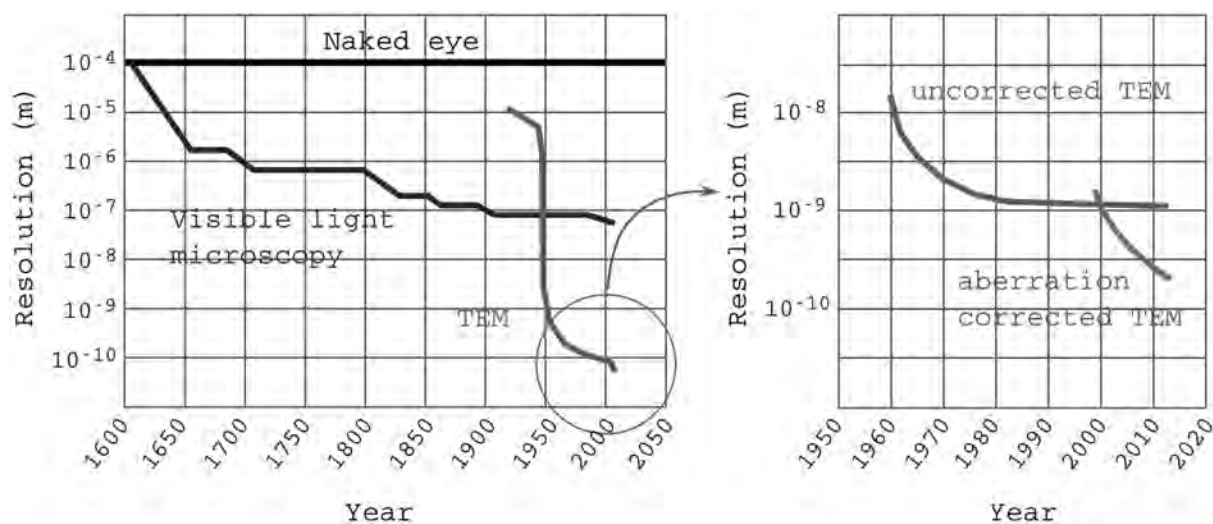


Figure 1. Evolution over time of the resolution achievable with the naked eye, a visible light microscope, and a transmission electron microscope. The saturation reached for visible light microscopy corresponds to the diffraction limit given by wavelength. For TEM, technical improvements such as aberration correctors (closeup in the right-hand side panel) are still pushing the resolution limit towards the diffraction limit.

accordingly in order to avoid wasting the effects of the correction.

### Where does contrast in the TEM come from?

In terms of linear optics, what a transmission microscope does is transform each point in the specimen into another object (a spread disk) in the final image. Defining the object as and the final image as , the latter can be defined as the convolution of the object transmission function with a point-spread function that represents the role of the microscope:

$$g(\vec{r}) = \int f(\vec{r}')h(\vec{r} - \vec{r}')d\vec{r}' = f(\vec{r}) \otimes h(\vec{r}) \quad (1)$$

A general definition of the object transmission function would be

$$f(x,y) = A(x,y) \cdot e^{-i\phi t(x,y)} \quad (2)$$

with amplitude  $A(x,y)$  and phase  $\phi_i(x,y)$ . The modulation of the electron beam transmitted through the sample can, thus, occur both in the amplitude and in the phase of the electron wave.

### Amplitude contrast

Let us first consider the effect on the amplitude of the electron wave of the scattering by the sample. Amplitude contrast manifests itself in two different forms: mass-thickness contrast, and diffraction contrast. Variations of mass and/or thickness of the specimen in conventional, parallel beam TEM give a contrast that can be understood in a similar way as absorption in visible light transmission microscopy. The role of optical absorption would be played in the TEM by the loss of intensity by scattering of the electrons, the process being governed by the Rutherford cross section for scattering by atomic nuclei. Diffraction contrast images use electrons coherently scattered at different Bragg conditions to obtain images with particular structural information on the specimen.

### Mass contrast: heavier vs lighter

Mass-thickness contrast can be described through the Rutherford scattering cross section

$$\sigma_R = 1.62 \times 10^{-24} \left( \frac{Z}{E_0} \right)^2 \cot^2 \left( \frac{\theta}{2} \right) \quad (3)$$

for electrons elastically scattered by nuclei into angles  $> \theta$ , considering screening of nuclei charge by deep level electrons charge and relativistic corrections. The other dependencies are on the atomic number  $Z$  and the energy of incoming electrons  $E_0$ , determined by the accelerating voltage. From this cross section, one can see that scattering is strongly forward peaked. However, any quantitative information will come from the small fraction of electrons scattered at large angles, i.e., angles greater than those of Bragg scattering, so diffraction contrast will not contribute to the image. STEM high angle annular dark field (HAADF) images contain information on the mass-thickness of the specimen, reaching even atomic level resolution. By focusing the electron beam on a small enough probe and collecting the scattered electrons on an annular detector with a sufficiently large hole to avoid Bragg electrons ( $> 3^\circ$ ), the resulting intensity will depend only on  $Z$  and on the thickness of the specimen,  $t$ . If the thickness is constant, or changes in a way that can be determined, images can be interpreted in terms of atomic number maps, as shown in figure 2. Combined with aberration correction, the chemical sensitivity of HAADF imaging has been successfully used in the characterization of the structure of materials at atomic level. An exemplary case is the determination of the atomic positions of the cation species in the unit cell of the superconductor YBCO (Varela *et al.*, 2003).

However, the leap from qualitative analysis of HAADF images to quantitative interpretation has to be taken with caution.

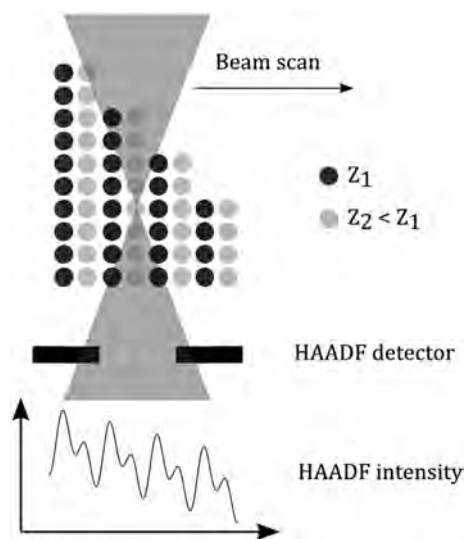


Figure 2. Schematic of a 1D HAADF acquisition. Effects of both atomic number and thickness in the HAADF intensity are illustrated.

STEM HAADF images provide useful information about the position of atomic columns in a crystal, and even about their composition through the Z dependence of contrast. However, lighter atoms such as oxygen or lithium, which are of great importance in many functional materials, are invisible to HAADF. The annular bright field (ABF) technique allows the detection of light atoms, in addition to the heavier ones, in STEM images. It can be thought of as a smart acquisition setting used in order to extract further information from the bright field (BF) imaging mode. It becomes particularly relevant in aberration-corrected STEM.

The signal collected on the BF detector has an annular distribution, despite being *inside* the direct illumination cone (as opposed to HAADF detectors). By placing a circular mask (the beam stopper) on the center of the beam, this angular distribution can be used in order to tune the contrast of the image. ABF images present negative, absorptive-type contrast (i.e., dark atomic columns) for a wide range of specimen thicknesses and defocus. To that extent, it is a robust technique with non-oscillating transfer functions, which makes image interpretation much easier, similar to the positive contrast in HAADF. The contrast enhancement for light atoms can be understood taking into account two main effects:

- Scattering by light atoms is strongly forward peaked towards the central BF region.
- Scattering by heavy atoms is stronger at large angles.

This angular scattering distribution was measured experimentally by Okunishi, Sawada and Kondo (2012) using the diffracting imaging technique, in which a diffraction pattern can be obtained with the STEM probe placed on a particular atomic column. The theoretical framework was proposed by Findlay, Okunishi, Sawada and Kondo (2010). The forward peaking of the scattering from light atoms can be explained by the dominance of the s-states channeling process. In this model, electrons couple to the s-type Bloch states, strongly localized around the atoms, and therefore, exit the specimen aligned with the direction of the atomic column. The scattering by heavier atoms is dominated by thermal diffuse scattering (TDS), resulting in larger scattering angles.

Considering the ABF signal as the subtraction of the central region integrated intensity from the large angle integrated intensity (given the non-coherence of STEM imaging), the subsequent darkening of the light atomic columns results in a global contrast en-

hancement: light atomic columns will i) appear darker against the background signal and ii) will not be shadowed by the contrast from heavier columns. On the downside, the resulting contrast will not have the additional chemical information found in HAADF images. However, if the experimental configuration consists in a purely annular bright field detector or a conventional bright field detector with a mask, it is straightforward to acquire ABF and HAADF signals simultaneously. This is not the case if the ABF conditions are achieved by a combination of large camera lengths and HAADF detectors.

### Diffraction contrast: orient your specimen in clever ways

Before getting down to real space imaging, let us first briefly describe how the electron beam is diffracted by the specimen in the TEM. Looking at a single unit cell in a crystalline material, the amplitude of the electron beam scattered by it can be expressed as

$$A_{cell} = \frac{e^{2\pi i \cdot \vec{k} \cdot \vec{r}}}{r} F(\theta) \quad (4)$$

where  $F(\theta)$  is the structure factor, containing information on the atomic number and relative positions of all the atoms in the unit cell. The amplitude of a beam diffracted at an angle  $\theta$  by  $n$  unit cells in the specimen will consist of a sum over those unit cells:

$$\phi_g = \frac{i\pi a}{\xi_g} \sum_n e^{2\pi i \vec{k} \cdot \vec{r}_n} \cdot e^{2\pi i \vec{k}_D \cdot \vec{r}} \quad (5)$$

where  $\vec{k}$  is defined as  $\vec{k} = \vec{k}_I - \vec{k}_D$ , the difference between the incident and the diffracted beams. A spot will appear in the diffraction pattern when  $k_D$  corresponds to scattering in a Bragg angle  $\theta_{Bragg}$ . The interplanar distance for the given plane family is  $a$ .  $\xi_g$  is the so called extinction distance for each diffraction vector  $g$ :

$$\xi_g = \frac{\pi V_c \cos \theta_{Bragg}}{\lambda F_g} \quad (6)$$

where  $V_c$  is the unit cell volume,  $\theta_{Bragg}$  is the Bragg angle,  $\lambda$  is the electron wavelength and  $F_g = F(\theta_{Bragg})$ . It is related to the unit cell dimension through  $V_c$ , its composition through  $F_g$ , and the accelerating voltage through  $\lambda$ . Notice that  $\xi_g$  does have dimensions of length and that the amplitude is, thus, dimensionless, as expected.

The electron beam inside the crystal can be thought of as a sum of the direct beam and all the diffracted beams, with amplitudes and respectively. As a con-

venient approximation for this description and also a practical situation in the microscope, let us consider the case where only the direct beam and one diffracted beam are present. In this two-beam approximation, only one family of planes is oriented in Bragg conditions. The change in amplitude for the direct and diffracted beams when going through the specimen ( $z$  direction) are described by the Howie-Whelan equations:

$$\frac{d\phi_g}{dz} = \frac{\pi i}{\xi_g} \phi_0 e^{2\pi i s z} + \frac{\pi i}{\xi_0} \phi_g \quad (7a)$$

$$\frac{d\phi_0}{dz} = \frac{\pi i}{\xi_0} \phi_0 + \frac{\pi i}{\xi_g} \phi_g e^{2\pi i s z} \quad (7b)$$

These coupled differential equations describe the continuous (dynamic) exchange of intensity between the direct and diffracted beam. Parameter  $s$  is called the excitation error, and corresponds to the distance from the diffracted beam  $k$ -vector to the reciprocal lattice node  $G$ , as described in figure 3.

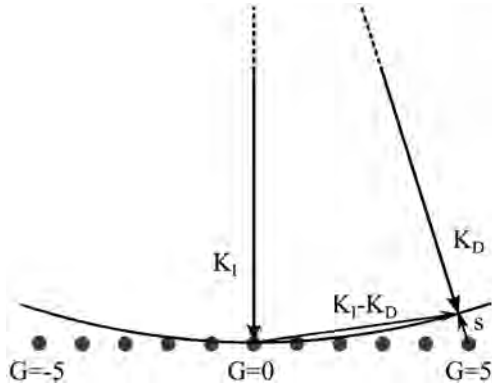


Figure 3. Schematic view of the diffraction of the electron beam by the crystal lattice.

Solving the Howie-Whelan equations under two-beam conditions yields the amplitude of any diffracted beam when in perfect two-beam conditions. Then, the actual intensity recorded in the diffraction pattern can be calculated as the squared modulus of this amplitude:

$$|\phi_g|^2 = \left( \frac{\pi t}{\xi_g} \right)^2 \frac{\sin^2(\pi t s_{eff})}{(\pi t s_{eff})^2} \quad (8)$$

where  $s_{eff}$  is an effective excitation error including the effect of the extinction distance of the particular reflection  $G$ :

$$s_{eff} = \sqrt{s^2 + \frac{1}{\xi_g^2}} \quad (9)$$

The diffraction intensity distribution is found at the back focal plane of the objective lens of the TEM. In diffraction mode, the image formation system of the TEM is used to transfer the information on this plane to the detector in order to obtain a diffraction pattern. In image mode, however, the objective aperture in this back focal plane can be used to obtain images with diffraction contrast.

A first distinction has to be made between bright field (BF) and dark field (DF) imaging, depending on whether the direct beam is included or excluded by the objective aperture. If we set the experimental two-beam conditions as discussed before, a *strong beam* DF image is formed by placing the objective aperture around the  $G$  reflection. Since electrons on that diffracted beam have been coherently scattered by a given  $(hkl)$  family of planes, areas in the image with those planes in zone axis will show bright (diffraction) contrast.

As can be seen from equation 8, the parameters that give rise, and therefore can modulate, diffraction contrast in the TEM are changes in thickness, through  $t$ , and changes in the diffracting conditions, through  $s$ . A non-uniform thickness will cause the presence of thickness fringes in the image, according to the sinusoidal dependence in equation 8. A local change in the orientation of the  $(hkl)$  planes will cause a tilt with respect to the incident beam and the apparition of bend contours. The latter is a key point in the diffraction imaging of defects in a material. Defects can bend, rotate, or modify the orientation of certain planes in and out of Bragg conditions. These changes can be imaged using diffraction contrast, thus mapping the variation of the excitation error  $s$  across the specimen.

The presence of defects in the crystal, either planar (grain boundaries, stacking faults, etc.) or linear, introduces a translation vector in the exponential terms of the Howie-Whelan equations.

In the particular case that the defect is out of contrast (invisibility criterion), the strong reflection to be used in a given orientation must be carefully selected.

In particular, the presence of strain fields around defects indicates the bending of the lattice planes, modifying the Howie-Whelan equation with a continuous variation of  $R$  with respect to  $z$ . The core of the dislocation is located at the  $R$  (o) position.

The excitation error will also change with  $R$  as

$$s_R = s + \vec{g} \cdot \frac{d\vec{R}}{dz} \quad (10)$$

Setting up a condition with a positive but small  $s$ , and placing the objective aperture around the  $G$  reflection, the resulting DF image will present strong

bright contrast at the areas where the defect brings the planes back into Bragg condition. The complementary BF image will present a dark contrast in the defect regions, where the planes are not in Bragg condition.

The previous description considers the use of strongly excited reflections to form the diffraction contrast image. However, using weakly excited reflections can provide useful information too, in the so called weak-beam dark-field mode. By placing the objective aperture in a reflection with a large excitation error  $s$ , the image will show bright contrast in the areas in which the defect bends the lattice back to Bragg conditions. A significant amount of intensity is lost, since it decays as  $\sim 1/s^2$ . The difference with respect to the strong beam situation is that the large value of  $s$  means a small coupling of the direct and diffracted beams, so  $\xi_{\text{eff}}$  is diffracted more kinematically. Moreover,  $\xi_{\text{eff}}$  will be small, so the defects will be imaged more sharply and with an intensity independent of  $\xi_{\text{eff}}$ .

#### Phase contrast: looking all the way down

Let us now consider the phase term in equation 2. Since we are considering only the phase contribution to contrast in the image, we can arbitrarily set  $A$  to 1. Given the small specimen thickness constraint for TEM observation, we are able to express the 3D electrostatic potential in the specimen as a 2D projected potential:

$$V_t(x, y) = \int_0^t V(x, y, z) dz \quad (11)$$

Electrons in the vacuum (i.e., outside the specimen) have an energy corresponding to the accelerating potential of the microscope,  $eV_{\text{acc}} = E$ . Electrons within the sample will have this energy modified by the projected potential,  $E + V(x, y, z)$ , at each thickness level in the beam propagation direction,  $dz$ . This change in energy can be related to a change in wavelength that causes a change in the phase of the electron wave going through each thickness level  $dz$ :

$$d\Phi = 2\pi \left( \frac{1}{\lambda'} - \frac{1}{\lambda} \right) dz \quad (12)$$

Taking into account the relationship between accelerating voltage and electron wavelength, this phase shift can be expressed in terms of electron energy and wavelength:

$$d\Phi = \frac{\pi}{\lambda E} V(x, y, z) = \sigma V(x, y, z) \quad (13)$$

where  $\sigma$  is called the interaction constant. Then, the total phase shift of the electron wave after going through the whole thickness of the specimen is

$$\Phi = \sigma \int_0^t V(x, y, z) dz = \sigma V_t(x, y) \quad (14)$$

We can introduce this expression for the phase shift in the object transmission function (Eq. 1.2). Considering again the small thickness of the sample, we can truncate the Taylor series expansion of this function at first order to get the weak-phase object approximation. In this approximation, the image function, as described in the linear image model (Eq. 1.1), can be expressed as

$$g(x, y) = [(1 - i\sigma V_t(x, y)) \otimes h(x, y)] \quad (15)$$

It is easier to work with the Fourier transform of  $h(x, y)$ . Equation 1 can be expressed in terms of Fourier transforms ( $G(k) = \text{FT}[g(r)]$ ,  $F(k) = \text{FT}[f(r)]$  and  $H(k) = \text{FT}[h(r)]$ ). According to the convolution theorem, convolutions in real space correspond to scalar products in Fourier (or frequency) space:

$$G(k) = F(k) \cdot H(k) \quad (16)$$

The main contribution to  $H(k)$  or *contrast transfer function*, comes from the aberrations of the optical system. Aberrations cause the electron wave to deviate from the ideal spherical wave front by a certain angular value,  $\alpha$ . Assuming a perfect rotational symmetry of the electromagnetic lens, the only possible aberrations are defocus ( $\Delta f$ ) and spherical aberration ( $C_s$ ). The change in phase due to these two aberrations can be expressed as

$$\chi(\alpha) = \frac{2\pi}{\lambda} \left( \frac{1}{4} C_s \alpha^4 - \frac{1}{2} \lambda \Delta f \alpha^2 \right) \quad (17)$$

Since angular deviation and frequency can be related via the electron wavelength ( $\alpha = \lambda \cdot k$ ), equation 17 can be expressed in terms of  $k$  as

$$\chi(k) = \pi \lambda k^2 \left( \frac{1}{2} C_s \lambda^2 k^2 - \lambda \Delta f \right) \quad (18)$$

The role of the contrast transfer function will be to modulate different spatial frequencies (i.e., different spacings in direct space) by a complex function of the form

$$H(k) = e^{-i\chi(k)} = (\cos[\chi(k)] - i \sin[\chi(k)]) \quad (19)$$

The actual image  $g(x, y)$  recorded in the microscope detector will be the intensity, i.e., the squared

modulus of the electron wave function after propagating through the specimen convoluted with the point spread function. Then, from equation 15 we have

$$g(x, y) = \psi \psi^* = |1 - i\sigma V_i(x, y) \otimes h(x, y)|^2 \approx 1 + 2\sigma V_i(x, y) \otimes h(x, y) \quad (20)$$

Considering the weak-phase object approximation, there is no contribution from the amplitude (cosine) term in the complex contrast transfer function in equation 19. Only the phase term (sine) remains:

$$H(k) = \sin[\chi(k)] \quad (21)$$

From this oscillatory behavior of the contrast transfer function we can see that different spatial frequencies, i.e., different spacings in the specimen, can be transmitted to the image with different intensities. To prevent the contrast transfer function from changing sign, an objective aperture can be placed in the back focal plane of the objective lens, selecting only spatial frequencies before the first zero of  $H(k)$ . Although the value of defocus can be optimized to have a region of uniformly transmitted contrast as large as possible, the so-called Scherzer defocus (see figure 4), contrast transfer will never be completely flat, and phase contrast HRTEM images will always require a careful interpretation.

Even if the effect of an objective aperture is not included in the CTF shown in figure 4, it can be seen that the contrast transfer goes to zero at a given spatial frequency. This is caused by both spatial and temporal incoherence of the illumination, each of them being responsible for an envelope function damping the CTF. Spatial incoherence is introduced by the finite (non-zero) size of the electron source. Temporal incoherence effects can be introduced by instabilities of the accelerating voltage, resulting in electrons with slightly different energies. Since the Scherzer defocus is the condition at which the homogeneous contrast transfer extends to the highest possible spatial frequency, the corresponding real space distance can be used as a way to define the point-resolution of the instrument. However, higher spatial frequencies are still transmitted up to the point at which either the temporal or spatial envelope functions damp the CTF to zero.

That spatial frequency is called the *information limit* of the instrument. Different approaches exist in order to try to extend the point resolution up to the information limit. From an instrumental point of view, electron holography was devised by Gabor (1948) as a way to suppress the effect of the aberrations in the objective system and, therefore, keep only the specimen-dependent modification of the electron wave, both in amplitude and phase. From an off-line data processing approach, exit wave reconstruction

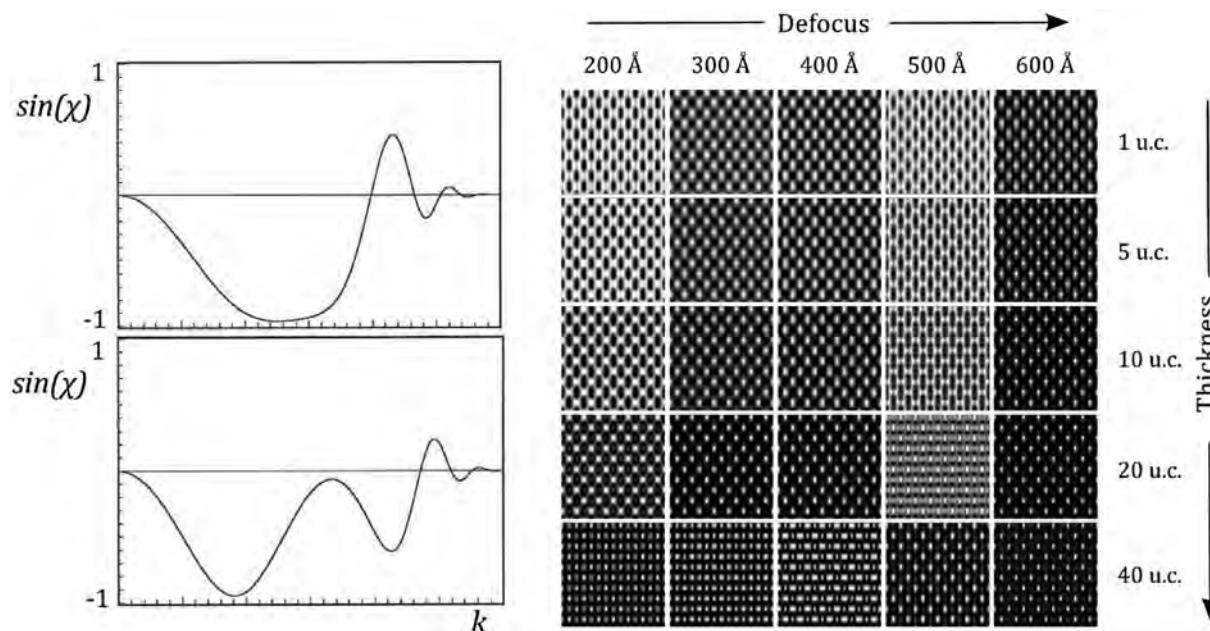


Figure 4. a) Phase distortion function in Scherzer (top) and out of Scherzer defocus (bottom) conditions. Contrast is transferred as positive or negative depending on the spatial frequency value  $k$ . b) Panel of 25 simulated images of a Si(110) crystal. Depending on the focus and the sample thickness, atoms appear bright or dark.

techniques use an acquired HRTEM through-focus series in order to mathematically calculate the effect of the aberrations of the objective system and suppress it. A new image can be generated with higher spatial resolution than any of the acquired images in the series. Two main procedures are used to retrieve the full electron wave (amplitude and phase). The first one relies on the Fourier analysis of the focal series in order to filter out the components that are not sample dependent. The second approach is the iterative modification of the exit wave and comparison with an initial phase guess or simulated electron wave, via the minimization of an error function. Given the fairly small degree of incoherence of the FEG guns and the readily available computational power, the iterative methods are the most commonly used.

We have shown that, even in a scenario with the simplest conditions, we can find atoms as both bright or dark spots in HRTEM images and that, even if the sign is maintained, the intensity recorded will not necessarily be proportional to physical, chemical or structural parameters of the sample. This effect of the contrast transfer function of the microscope has been responsible for keeping HRTEM an almost completely qualitative technique for a long time. In the past few years, however, tools that allow extracting quantitative information from HRTEM images have become more accessible.

### Relevance of advanced TEM modes for materials science

In this introduction to the basic working principles of TEM, the power of the instrument as an ultimate image resolution tool has been established. Stemming from this central aspect, a variety of TEM-related techniques are devoted to revealing properties of materials at the spatial resolution that TEM can provide. Either by the adequate processing of images, the use of particular instrumental configurations, or the addition of the needed detectors, it is possible to obtain information crucial to solving challenging materials science problems. Some of these properties, of particular interest in the present thesis, are summarized in figure 5.

Being able to directly relate the final properties with the intimate structure provides unique insight into the functionality of materials and devices, especially when compared to the necessarily statistical nature of information that can be gathered through macroscopic measurements. The role of defects as non-radiative recombination centers in semicon-

ductors, the free surface structure in oxides for gas sensing, or the local magnetic configuration of nanoparticle assemblies for magnetic hyperthermia, for instance, need to be assessed through TEM techniques, which can unveil the local information needed to understand the macroscopic behavior of these systems.

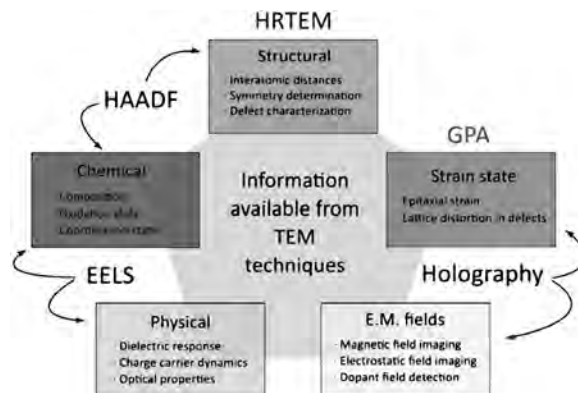


Figure 5. Materials properties, as related to TEM techniques.

In particular, the scale reduction associated with the nanoscience and nanotechnology revolution demands characterization tools capable of reaching an unprecedented resolution, in a wide range of fields, not only for standard quality control, but in order to understand the properties of matter at the nanoscale. Going from bigger to smaller devices, but also from elemental building blocks (even atoms) to bigger assemblies, basic properties and device functionalities meet. With its ability to provide different kinds of information at a very high spatial resolution, state-of-the-art TEM and related techniques are at the core of this multidisciplinary and rapidly growing field.

### Bibliography

- ALLPRESS, J. G.; SANDERS, J. V.; WADSLEY (1969). "Multiple Phase Formation in the Binary System Nb<sub>2</sub>O<sub>5</sub>-WO<sub>3</sub>. VI Electron Microscopic Observation and Evaluation of Non-Periodic Shear Structures". *Acta Cryst. Section B*, no. B25.
- BROGLIE, L. DE (1925). "Recherches sur la théorie des quanta". *Ann. de Phys.*, 10e série, t. III.
- CLIFF, G.; LORIMER, G. W. (1975). "The Quantitative Analysis of Thin Specimens". *Journal of Microscopy*, no. 103 (2).
- COWLEY, J. M. (1969). "Image Contrast in a Transmission Scanning Electron Microscope". *Appl. Phys. Lett.*, no. 15 (58).
- CREWE, A. V.; ISAACSON, M.; JOHNSON, D. (1969). "A Simple Scanning Electron Microscope". *Rev. Sci. Instrum.*, no. 40 (241).
- EGERTON, R. F. (2011). *Electron Energy Loss Spectroscopy in the Electron Microscope*. Springer, 3rd ed.

- FINDLAY, S. D.; OKUNISHI, E.; SAWADA, H.; KONDO, Y. (2010). "Dynamics of Annular Bright Field Imaging in Scanning Transmission Electron Microscopy". *Ultramicroscopy*.
- GABOR, D. (1948). "A New Microscopic Principle". *Nature*, no. 777 (4098).
- HAIDER, M.; UHLEMANN, S.; SCHWAN, E.; ROSE, H.; KABIUS, B., URBAN, K. (1998). "Electron Microscopy Image Enhanced". *Nature*, no. 392 (768).
- HOWIE, A.; WHELAN, M. J. (1961). "Diffraction Contrast of Electron Microscope Images of Crystal Lattice Defects. II The Development of a Dynamical Theory". *Proc. Roy. Soc.*, no. A263.
- KNOLL, M.; RUSKA, E. (1931). "The Electron Microscope". *Z. Physik*, no. 12 (78).
- (1932). "Geometric Electron Optics". *Ann. Physik*, no. 12 (607).
- OKUNISHI, E.; SAWADA, H.; KONDO, Y. (2010). "Experimental Study of Annular Bright Field (ABF) Imaging Using Aberration Corrected Scanning Transmission Electron Microscopy (STEM)". *Micron*, no. 20.
- SCHERZER, O. (1936). "Über einige Fehler von Elektronenlinsen". *Zeitschrift für Physik*, no. 101 (9-10).
- (1947). "Sphärische und chromatische Korrektur von Elektronenlinsen". *Optik*, no. 2.
- VARELA, M.; LUPINI, A. R.; PENNYCOOK, S. J.; SEFRIQUI, Z.; SANTAMARÍA, J. (2003). "Nanoscale Analysis of YBa<sub>2</sub>Cu<sub>3</sub>O<sub>7-x</sub>/LaO<sub>0.67</sub>Ca<sub>0.33</sub>MnO<sub>3</sub> Interfaces". *Solid-State Electronics*, no. 47.
- WATANABE, M.; WILLIAMS, D. B. (2006). "The Quantitative Analysis of Thin Specimens: A Review of Progress from the Cliff-Lorimer to the New Zeta-Factor Methods". *Journal of Microscopy*, no. 221.

